Unsupervised polarimetric SAR image segmentation and classification using region growing with edge penalty

Peter Yu, A. K. Qin, *Member, IEEE,* David A. Clausi, *Senior Member, IEEE*

***Abstract*—A region-based unsupervised segmentation and classification algorithm for polarimetric SAR imagery that incorporates region growing and a Markov random field (MRF) edge strength model is designed and implemented. This algorithm is an extension of the successful Iterative Region Growing with Semantics (IRGS) segmentation and classification algorithm, which was designed for amplitude only SAR imagery, to polarimetric data. Polarimetric IRGS (PolarIRGS) extends several aspects of IRGS by incorporating a polarimetric feature model based on the Wishart distribution and modifying key steps such as initialization, edge strength computation and the region growing criterion. Like IRGS, PolarIRGS oversegments a SAR image into regions and employs iterative region growing to reduce the size of the solution search space. The incorporation of an edge penalty in the spatial context model improves segmentation performance by preserving segment boundaries that traditional spatial models will smooth over. Evaluation of PolarIRGS with Flevoland fully polarimetric data shows that it improves upon two other recently published techniques in terms of classification accuracy.**

***Index Terms*—synthetic aperture radar (SAR), image segmentation, complex, polarimetry, Markov random field (MRF), Wishart, region-based**

I. Introduction

POLARIMETRIC synthetic aperture radar (SAR) imagery provides useful information in a diverse number of applications from sea ice monitoring [1], [2] to land cover classification [3] and agricultural crop identification [4]. There is now an increasing volume of fully polarimetric data available due to the launch of sensors capable of fully-polarimetric imaging such as RADARSAT-2. Therefore, automated image segmentation and classification methods are desired in order to replace manual interpretation, which remains subjective and labour-intensive.

Automated segmentation and classification of fully polarimetric SAR imagery has been an ongoing field of research. Maximum likelihood classifiers based on the assumption that classes are Wishart distributed have been developed [5]–[7]. An alternative approach [8], based on the assumption that classes are modelled by complex Gaussian distributions, additionally incorporates a Markov random field (MRF) spatial context model that can overcome some of the effects of noise by smoothing the segmentation according to the local interactions between pixel labels. A recent work [9] uses a non-parametric estimate of the class distributions in addition to a modified spatial context model that attempts to prevent over-smoothing of the segmentation result across true class boundaries.

The previously mentioned papers perform segmentation on a per-pixel basis. However, region-based segmentation methods also exist and are advantageous because they reduce the computation demand working on regions instead of pixels, they help the optimization procedure converge more effectively to the global solution, and they help to alleviate problems with noisy imagery by using region statistics instead of values of individual pixels. Several recent papers advocate region-based image segmentation. Wu et al. [10] use a Wishart distribution with a region-based MRF framework for segmentation. The image is first oversegmented into square regions, which are then iteratively refined by a Wishart MRF (WMRF) model. The refined regions are then classified with training data. Wu et al.'s technique uses only a basic MRF spatial context model which penalizes all class boundaries equally, including true class boundaries which should not be penalized.

Agglomerative hierarchical clustering [11] is another technique that oversegments the image into many regions (based on clustering over a polarimetric decomposition data space) followed by region merging to produce the final segmentation. Spectral graph partitioning [12] (SGP) is a recent technique in which the image is first segmented into regions with contour information and spatial proximity and the regions are then grouped by spectral clustering. Neither agglomerative hierarchical clustering [11] nor SGP [12] include a spatial context model to improve segmentation results, although SGP makes use of edge information in the image.

The advantage of a region-based approach combined with an MRF spatial context model has been demonstrated for non-polarimetric SAR imagery by the recent Iterative Region Growing with Semantics (IRGS) algorithm [13], which has outperformed other algorithms when applied to amplitude-only SAR images of sea ice [14], generic imagery [15] and optical imagery of savannah wetlands [16]. IRGS incorporates edge strength between regions as part of the spatial context model to ensure that true class boundaries are preserved as regions grow using a merging criterion. This is similar to the segmentation energy function defined in [17] but IRGS incorporates a different type of edge strength penalty function to aid in the segmentation process [13]. IRGS is an unsupervised

Manuscript received ; revised .

The Natural Sciences and Engineering Research Council (NSERC) of Canada, NSERC International Polar Year (IPY) and GEOIDE (Geomatics for Informed Decisions, a Network of Centres of Excellence) financially supported this work.

The authors are members of the Vision and Image Processing (VIP) research group in the Department of Systems Design Engineering, University of Waterloo, Waterloo, ON, N2L 3G1 Canada.

algorithm, meaning that no training data is necessary prior to segmentation and classification.

This paper presents an extension to IRGS for polarimetric SAR imagery. By combining the successful region-based approach and edge-strength spatial context model of IRGS with the Wishart distribution model, unsupervised polarimetric scene segmentation and classification can be improved.

Section II presents information about polarimetric SAR imagery, image segmentation, classification and the IRGS algorithm. Section III details the extension of IRGS to Polarimetric IRGS (PolarIRGS). Section IV describes the test data set. Section V presents the results of PolarIRGS as applied to real fully polarimetric imagery. Conclusions and recommendations for future work follow in Section VI.

II. BACKGROUND

A. Polarimetric SAR images

A fully polarimetric radar measures the complex scattering matrix of the target medium, which in the monostatic case with a reciprocal medium reduces to a complex scattering vector [5]:

$$\mathbf{u} = \begin{bmatrix} S_{hh} & \sqrt{2}S_{hv} & S_{vv} \end{bmatrix}^T \tag{1}$$

The terms S_{hh}, S_{hv}, S_{vv} correspond to the complex scattering coefficients of the HH, HV and VV polarizations, respectively. Multi-look processing is often performed for speckle reduction and data compression of SAR data by averaging several single-look outer products $\mathbf{u}\mathbf{u}^\dagger$ [18]:

$$\mathbf{Z} = \frac{1}{n}\sum_{k=1}^{n} \mathbf{u}_k \mathbf{u}_k^\dagger \tag{2}$$

where n is the number of looks, $\mathbf{u}_k$ is the k^{th} single-look scattering vector and † is the conjugate transpose operator. The polarimetric covariance matrix $\mathbf{Z}$, or a measure that can be converted to it, is the measurement provided at each pixel from a multi-look, polarimetric image. The matrix $\mathbf{A} = n\mathbf{Z}$ has a complex Wishart [19] distribution [18]:

$$p(\mathbf{A}) = \frac{|\mathbf{A}|^{n-q} \exp\left(-\text{tr}(\mathbf{C}^{-1}\mathbf{A})\right)}{K(n,q)|\mathbf{C}|^n} \tag{3}$$

where $|\mathbf{A}|$ is the determinant of $\mathbf{A}$, $\text{tr}(\mathbf{C}^{-1}\mathbf{A})$ is the trace of $\mathbf{C}^{-1}\mathbf{A}$, $\mathbf{C} = \text{E}[\mathbf{u}\mathbf{u}^\dagger]$ and:

$$K(n,q) = \pi^{\frac{1}{2}q(q-1)} \prod_{i=1}^{q} \Gamma(n-i+1) \tag{4}$$

The value of q is the number of elements in $\mathbf{u}$ and Γ is the Gamma function. In the case of monostatic polarimetric radar, $q = 3$ under the reciprocity assumption [18]. For the Wishart distribution in Eq. (3) to be nonsingular, $n \geq q$. Eq. (3) will be used in Section III to develop PolarIRGS.

B. Region-based Image Segmentation Problem Definition

Let $\mathcal{C}$ be the number of segmented classes in the image. Let $\mathcal{S} = \{(i,j)|1 \leq i \leq M, 1 \leq j \leq N\}$ represent a discrete two dimensional rectangular lattice of size M rows $\times$ N columns (i.e. an M row $\times$ N column image) and let $s \in \mathcal{S}$ represent a site in the lattice (i.e. a pixel in the image). Let $\mathbf{X} = \{X_s | s \in \mathcal{S}\}$ be a set of discrete random variables forming a random field on $\mathcal{S}$, with each X_s taking a value from $\mathcal{L} = \{1, \ldots, \mathcal{C}\}$ that indicates the class label of site s. Also, let $\mathbf{Y} = \{\mathbf{Y_s} | s \in \mathcal{S}\}$ be a random field on $\mathcal{S}$. Each $\mathbf{Y_s}$ represents a measurement at site s and can take on a scalar, vector or matrix value. For the polarimetric data in this paper, each $\mathbf{Y_s}$ takes on a positive definite Hermitian matrix which represents the complex covariance matrix $\mathbf{Z}_s$ measured at site s (see Eq. (2)).

Label field configuration $\mathbf{x} = \{x_s | x_s \in \mathcal{L}, s \in \mathcal{S}\}$ and observed image $\mathbf{y} = \{\mathbf{y}_s | s \in \mathcal{S}\}$ are realizations of $\mathbf{X}$ and $\mathbf{Y}$, respectively. The domain of $\mathbf{y}_s$ depends on the type of image data being considered: for a multichannel image with d bands, $\mathbf{y}_s$ are d-dimensional vectors (i.e., $\mathbf{y} = \{\mathbf{y}_s | \mathbf{y}_s \in \mathbb{R}^d, s \in \mathcal{S}\}$), while for multi-look polarimetric data, $\mathbf{y} = \{\mathbf{Z}_s | s \in \mathcal{S}\}$, where the domain of $\mathbf{Z}_s$ is the cone of positive definite Hermitian matrices [18].

Image segmentation involves finding an optimal $\mathbf{x}$ according to some criteria on $\mathbf{x}$ and $\mathbf{y}$. After segmentation, $\Omega_1, \ldots, \Omega_C$ are disjoint subsets of $\mathcal{S}$ that denote the $\mathcal{C}$ classes in the label field configuration $\mathbf{x}$. Image segmentation, as defined here, allows classes that consist of unconnected regions. This definition of image segmentation is consistent with that given by Gonzalez and Woods [20, p. 690] and Li [21, p.188] and has been used in other published work [11] [9] [22]. By allowing classes that consist of unconnected regions and by not using any training data to find the optimal $\mathbf{x}$, the segmentation result is also an unsupervised classification result. Each of the regions is a connected image segment with a classification label assigned. The proposed PolarIRGS algorithm can therefore be considered a *combined* unsupervised segmentation *and* classification algorithm. It is a region-based method based on the IRGS algorithm [13], in which an image is represented as a region-adjacency graph (RAG) [23]. Under a RAG representation, the image is first oversegmented into a number of disjoint and relatively homogeneous regions that comprises more than one image site and the label field is defined over the RAG [24] instead of the lattice $\mathcal{S}$.

A RAG is represented as $\mathcal{G} = (\mathcal{V}, \mathcal{E})$, where $\mathcal{V}$ denotes the set of image regions as vertices of the graph and $\mathcal{E}$ denotes the set of arcs that connect spatially adjacent regions. A region $v \in \mathcal{V}$ represents an image region and $\mathcal{S}_v$ denotes the set of image sites belonging to region v. An arc $e \in \mathcal{E}$ represents the shared boundary between two adjacent regions. The random field for the label configuration is now defined on $\mathcal{G}$ [24] and is denoted by $\mathbf{X^r} = \{X_v^r | X_v^r \in \mathcal{L}, v \in \mathcal{V}\}$, where the superscript 'r' denotes a region-based definition of each term. The region-based label field configuration $\mathbf{x}^r = \{x_v^r | x_v^r \in \mathcal{L}, v \in \mathcal{V}\}$ is a realization of $\mathbf{X}^r$. Here, x_v^r denotes the label for all sites $s \in \mathcal{S}_v$.

All regions are mutually separated by region boundaries, which are comprised of image sites that are not part of any

regions. The division of image sites into boundary sites and sites that are part of regions follows several rules [25, Sec. 4.2.1]. All sites in the image are either boundary sites or part of a region and sites that are a part of one region cannot be a part of any other regions. Additionally, only sites that separate two regions are boundaries. An arc on the RAG connects regions v and w if they share a common boundary. These rules generate the following formal definition of regions and boundary sites [25, Sec. 4.2.1]:

1) $\bigcup_{v\in\mathcal{V}} \mathcal{S}_v \bigcup_{v\in\mathcal{V}} \partial\mathcal{S}_v = \mathcal{S}$
2) $\forall v, w : \mathcal{S}_v \bigcap \partial\mathcal{S}_w = \emptyset$
3) $\forall v \neq w : \mathcal{S}_v \bigcap \mathcal{S}_w = \emptyset$
4) $\forall v : \partial\mathcal{S}_v \subseteq \bigcup_{w\in\mathcal{V}, w\neq v} \partial\mathcal{S}_w$

where $\partial\mathcal{S}_v$ is a one-pixel boundary outlining region $\mathcal{S}_v$. Regions v and w share a common boundary if $\partial\mathcal{S}_v \cap \partial\mathcal{S}_w \neq \emptyset$.

There are fewer possible configurations of the region-based label field $\mathbf{x}^r$ than the pixel-based field as there are far fewer regions than pixels. In Section II-C, it will be seen that MRF-based segmentation problems are a combinatorial optimization problem. Therefore, the region-based approach reduces the solution search space, leading to better optimization results. Additionally, region-based segmentation reduces the negative effects of variation and noise within each region on the image segmentation result.

C. IRGS Algorithm

This section provides a high level explanation and summarizes the details of the IRGS algorithm to provide context for understanding the polarimetric extension in this paper. Additional details are described in previously published papers [13] [15]. Assuming that $\mathbf{X^r}$ is an MRF with respect to a certain neighbourhood system on RAG $\mathcal{G}$, the unsupervised image segmentation and classification problem is formulated as finding the label field configuration $\mathbf{x}^{r*}$ that satisfies [15] [21]:

$$\mathbf{x}^{r*} = \arg\max_{\mathbf{x}^r\in\mathbf{X^r}} p(\mathbf{y}|\mathbf{x}^r)P(\mathbf{x}^r) \tag{5}$$

where $p(\mathbf{y}|\mathbf{x}^r)$ is the conditional probability density function of the observed image $\mathbf{y}$ given the specific label field configuration $\mathbf{x}^r$ and $P(\mathbf{x}^r)$ is the probability of a specific label configuration and is defined by the specific MRF model chosen [21]. The operator $\arg\max$ selects the label field configuration $\mathbf{x}^r$ that maximizes $p(\mathbf{y}|\mathbf{x}^r)P(\mathbf{x}^r)$. The selected label field configuration is denoted by $\mathbf{x}^{r*}$, where the superscript $*$ indicates that $\mathbf{x}^{r*}$ is the optimal configuration with respect to Eq. 5. The term $p(\mathbf{y}|\mathbf{x}^r)$ is called the feature model because it models the distribution of the features (the observation values in $\mathbf{y}$) based on $\mathbf{x}^r$ and $P(\mathbf{x}^r)$ is called the spatial context model because it models the probability of the various possible configurations of $\mathbf{x}^r$, with some configurations being more likely under the chosen MRF model. Extending the IRGS algorithm to polarimetric data involves replacing the feature model and adapting the spatial context model to match the characteristics of polarimetric data.

Under a class-conditionally independent assumption, $p(\mathbf{y}|\mathbf{x}^r)$ can be written as:

$$p(\mathbf{y}|\mathbf{x}^r) = \prod_{i=1}^{\mathcal{C}} \prod_{\mathcal{S}_v\in\Omega_i} \prod_{s\in\mathcal{S}_v} p(\mathbf{y}_s|x_v^r = i) \tag{6}$$

where $\mathcal{S}_v \in \Omega_i$ selects the set of sites $\mathcal{S}_v$ for each region v that belongs to class i (i.e. $\{\mathcal{S}_v|\{v|x_v^r = i\}\}$). Although the segmentation is region-based, (6) is written in terms of image sites because the calculations are based on individual site values. The term $p(\mathbf{y}_s|x_v^r)$ describes the probability of obtaining value $\mathbf{y}_s$ given that the site belongs to the class specified by x_v^r. Note that under the region-based definition, $x_s = x_v^r$ for $s \in \mathcal{S}_v$.

In order to solve (5), it is converted into an energy function by taking the logarithm to change products into sums and changing the sign to give an equivalent minimization problem:

$$\mathbf{x}^{r*} = \arg\min_{\mathbf{x}^r\in\mathbf{X^r}} E_f(\mathbf{y}, \mathbf{x}^r) + E_s(\mathbf{x}^r) \tag{7}$$

where $E_f(\mathbf{y}, \mathbf{x}^r)$ is the feature model term corresponding to $p(\mathbf{y}|\mathbf{x}^r)$ and $E_s(\mathbf{x}^r)$ is the spatial context model term corresponding to $P(\mathbf{x}^r)$. $E_f(\mathbf{y}, \mathbf{x}^r)$ is derived for polarimetric data in Section III.

In IRGS, for a given region v, all regions that are connected to it by one arc in the RAG are considered neighbours. Under this MRF neighbourhood system, the spatial context model energy $E_s(\mathbf{x}^r)$ is [15]:

$$E_s(\mathbf{x}^r) = \beta \sum_{i=1}^{\mathcal{C}-1} \sum_{j=i+1}^{\mathcal{C}} \sum_{s\in\partial\Omega_i\cap\partial\Omega_j} g(\nabla_s) \tag{8}$$

where $g(\nabla_s)$ is the edge penalty term and $\partial\Omega_i$ comprises all the boundary sites that separate regions assigned to class i from regions assigned to other classes. Hence, $\partial\Omega_i \cap \partial\Omega_j$ selects the shared boundary sites between classes i and j. The parameter β controls the degree to which the spatial context model is weighted, with larger β resulting in smoother segmentations.

At a conceptual level, (8) penalizes segmentations where adjacent regions are assigned to different classes. For every boundary site that separates a region of class i from a region of class j, $E_s(\mathbf{x}^r)$ is increased by $\beta \cdot g(\nabla_s)$. The edge penalty term $g(\nabla_s)$ is a monotonically decreasing function of ∇_s, where $\nabla_s \in [0, 1]$ is a measure of the edge strength at site s. The penalty is smaller when there is a strong edge between two regions assigned to different classes than when the edge is weak. This approach favours assigning adjacent regions to the same class only when the edge between them is weak, recognizing that strong edges indicate true class boundaries.

The spatial context energy used in IRGS is similar to the spatial context energy in the multi-level logistic (MLL) [26] model except for the addition of the edge penalty term $g(\nabla_s)$. The MLL model may over-smooth across true class boundaries since all boundaries are penalized equally.

The edge penalty function $g(\nabla_s)$ used in IRGS is [15, Eq. (15)]:

$$g(\nabla_s) = \exp\left[-\left(\frac{\nabla_s}{K}\right)^2\right] \tag{9}$$

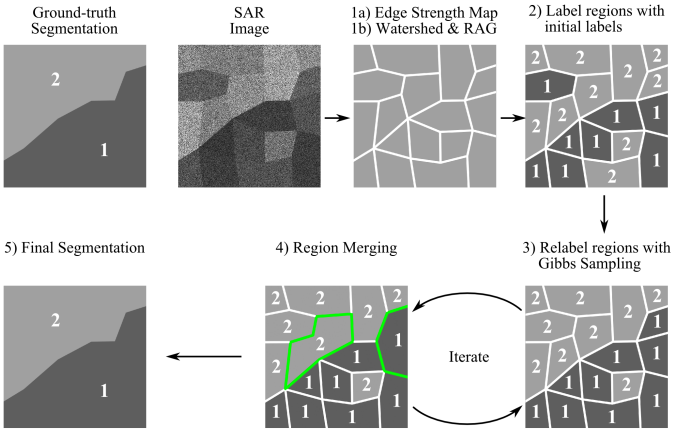

Fig. 1. Major steps of the IRGS algorithm. 1a) To initialize the system, IRGS computes the edge strength map and 1b) generates the watershed regions and the region adjacency graph (RAG) from the SAR image. The watershed regions have simplified shapes in this diagram and are more arbitrary in practice. 2) The watershed regions are then given initial labels. 3) Regions are relabelled by Gibbs sampling [28]. 4) Regions with the same label are merged. Steps 3 and 4 are repeated for a user-specified number of iterations. 5) The final segmentation is produced.

The only difference between $g(\nabla_s)$ for PolarIRGS and $g(\nabla_s)$ for IRGS [15] is the calculation of ∇_s for polarimetric data, which is described in Section III. The term K is a positive value that controls the strength of the edge penalty term (see [13, Sec. 3] for details).

IRGS iteratively searches for the configuration of labels that solves (7). At each iteration, IRGS incorporates a region-merging process on the intermediate segmentation to reduce the number of nodes in the RAG, which makes subsequent iterations more efficient and prevents the algorithm from becoming trapped in local minima in the solution space [13]. IRGS merges adjacent regions that have the same class label in a greedy fashion. It computes a merging criterion ∂E [13] for each eligible pair of regions and merges the pair with the most negative ∂E. This continues until no more negative ∂E are found. Shared boundary sites between two regions become absorbed into the merged region.

Fig. 1 shows the major steps of the IRGS algorithm. The algorithm starts by accepting an image as input. The image is first oversegmented with a watershed algorithm [27] using an edge strength map $\nabla = \{\nabla_s | s \in \mathcal{S}\}$. The RAG is then constructed with each watershed region becoming a vertex in the graph. Neither IRGS nor the proposed PolarIRGS is constrained to any particular oversegmentation algorithm for the construction of the RAG; the Vincent and Soille watershed algorithm [27] was chosen because it produces a reasonable RAG for both IRGS and the proposed PolarIRGS. After the RAG is constructed, each region is assigned an initial label to initialize IRGS. IRGS then enters its iterative portion. At each iteration, each region is assigned a label with Gibbs sampling [28] to move the label configuration toward the optimal solution. Regions are then merged and the next iteration of IRGS is executed.

The combined segmentation and classification nature of IRGS is apparent from the preceding high-level description. Each of the regions is an image segment which is assigned a generic label from $\mathcal{L} = \{1, \ldots, \mathcal{C}\}$ in an unsupervised fashion as no *a priori* data is provided other than the number of classes. The final output of IRGS is the label field configuration $\mathbf{x}^{r*}$, which is an unsupervised classification map of the scene.

III. Proposed Method

There are three main types of unsupervised classification algorithms for polarimetric SAR data [18]: statistical (e.g. clustering), physical and combined physical-statistical algorithms. The proposed PolarIRGS algorithm is an extension of the statistical type since it not only includes a statistical model, but also a spatial context model. Algorithms with physical models use domain knowledge such as the scattering characteristics of broad categories of surfaces (e.g. vegetation, buildings and water) to divide a scene into these categories. The combined physical-statistical algorithms use both physical models and statistical techniques. For example, Lee at el. [29] used a Freeman-Durden decomposition to divide a scene into three categories of scattering characteristics. Each category is then separately classified with a statistical clustering technique in an unsupervised fashion. This paper is focused on the development of statistical unsupervised classification. The use of novel statistical techniques such as PolarIRGS in a combined physical-statistical classification framework could be investigated in future work.

To implement PolarIRGS, the following details must be described:

A) Derivation of the feature model energy $E_f(\mathbf{y}, \mathbf{x}^r)$ in (7) for polarimetric data.
B) Definition of the region merging criterion ∂E.
C) Calculation of the edge strength measure ∇_s, which is used by both the watershed algorithm and the edge penalty function $g(\nabla_s)$ in (8).
D) Initialization method to assign initial labels to all regions.
E) Choice of spatial context weighting parameter β.
F) Model for labeling the boundary sites that remain after the region level label field configuration $\mathbf{x}^{r*}$ is generated to create the final segmentation and classification image $\mathbf{x}$.

A. Feature Model Energy

In (3), $p(\mathbf{A})$ can be restated as $p(\mathbf{A}_s | x_v^r = i)$ [5]:

$$p(\mathbf{A}_s | x_v^r = i) = \frac{|\mathbf{A}_s|^{n-q} \exp\left(-\text{tr}(\mathbf{C}_i^{-1}\mathbf{A}_s)\right)}{K(n,q)|\mathbf{C}_i|^n} \tag{10}$$

where $\mathbf{C}_i$ is the mean polarimetric covariance matrix of class i. This corresponds to the $p(\mathbf{y}_s | x_v^r = i)$ terms in (6), assuming that $\mathbf{y}_s = \mathbf{A}_s = n\mathbf{Z}_s$. In the actual data, $\mathbf{y}_s = \mathbf{Z}_s$ but this can be ignored for the derivation. The feature model energy $E_f(\mathbf{y}, \mathbf{x}^r)$ can be derived by substituting (10) into (6), taking the natural logarithm and changing the sign:

$$E_{f_1}(\mathbf{y}, \mathbf{x}^r) = \sum_{i=1}^{\mathcal{C}} \sum_{\mathcal{S}_v \in \Omega_i} \sum_{s \in \mathcal{S}_v} \{n \ln |\mathbf{C}_i| + \ln(K(n,q)) + \text{tr}(\mathbf{C}_i^{-1}\mathbf{A}_s) - (n-q)\ln|\mathbf{A}_s|\} \tag{11}$$

Eliminating all terms that are not a function of i and substituting $\mathbf{A}_s = n\mathbf{Z}_s$ into (11) gives [5]:

$$E_{f_2}(\mathbf{y}, \mathbf{x}^r) = \sum_{i=1}^{\mathcal{C}} \sum_{\mathcal{S}_v \in \Omega_i} \sum_{s \in \mathcal{S}_v} \{n \ln |\mathbf{C}_i| + n\text{tr}(\mathbf{C}_i^{-1}\mathbf{Z}_s)\} \quad (12)$$

The constant multiplier n can be dropped (which does not affect the validity of the energy value), giving the final feature model energy, in terms of $\mathbf{C}_i$ and $\mathbf{Z}_s$:

$$E_f(\mathbf{y}, \mathbf{x}^r) = \sum_{i=1}^{\mathcal{C}} \sum_{\mathcal{S}_v \in \Omega_i} \sum_{s \in \mathcal{S}_v} \{\ln |\mathbf{C}_i| + \text{tr}(\mathbf{C}_i^{-1}\mathbf{Z}_s)\} \quad (13)$$

The term in the sum is the Wishart distance measure derived by Lee et al. [5].

B. Region-merging criterion

The region-merging criterion ∂E determines whether two regions are to be merged during the region-merging stage. Region-merging considers a single pair of adjacent regions with the same class label at a time. Once a pair of eligible regions is selected, the algorithm determines the energy for a two region version of (7). In this modified version of (7), the energy is calculated with only the two regions being considered for merging. The energy for two cases is calculated [13]: 1) the two regions are separate classes (unmerged) and 2) the two regions are the same class (merged). If the energy is lower for the merged case, the regions are merged. Formally, IRGS merges regions v and w if $\partial E(v, w) < 0$, where:

$$\partial E(v, w) = E_{\text{merged}}(v, w) - E_{\text{unmerged}}(v, w) \quad (14)$$

The two energies in (14) have the following values for polarimetric data:

$$E_{\text{merged}}(v, w) = \sum_{s \in \mathcal{S}_v \cup \mathcal{S}_w} \{\ln |\mathbf{C}_{vw}| + \text{tr}(\mathbf{C}_{vw}^{-1}\mathbf{Z}_s)\} \quad (15)$$

$$\begin{aligned} E_{\text{unmerged}}(v, w) = &\sum_{s \in \mathcal{S}_v} \{\ln |\mathbf{C}_v| + \text{tr}(\mathbf{C}_v^{-1}\mathbf{Z}_s)\} + \\ &\sum_{s \in \mathcal{S}_w} \{\ln |\mathbf{C}_w| + \text{tr}(\mathbf{C}_w^{-1}\mathbf{Z}_s)\} + \\ &\beta \sum_{s \in \partial\mathcal{S}_v \cap \partial\mathcal{S}_w} g(\nabla_s) \end{aligned} \quad (16)$$

where $\mathbf{C}_v$ is the average polarimetric covariance matrix for region v and $\mathbf{C}_{vw}$ is the average covariance matrix for the union of regions v and w. Since $\mathbf{C}_v = \frac{1}{|\mathcal{S}_v|} \sum_{s \in \mathcal{S}_v} \mathbf{Z_s}$, where $|\mathcal{S}_v|$ indicates the cardinality of $\mathcal{S}_v$, $\partial E(v, w)$ can be simplified by making the following substitution into Eqs. 15 and 16 for v, w and vw:

$$\begin{aligned} &\sum_{s \in \mathcal{S}_v} \{\ln |\mathbf{C}_v| + \text{tr}(\mathbf{C}_v^{-1}\mathbf{Z}_s)\} \\ &= |\mathcal{S}_v| \ln |\mathbf{C}_v| + \text{tr}(\mathbf{C}_v^{-1} \sum_{s \in \mathcal{S}_v} \mathbf{Z}_s) \\ &= |\mathcal{S}_v| \ln |\mathbf{C}_v| + \text{tr}(\mathbf{C}_v^{-1} |\mathcal{S}_v| \mathbf{C}_v) \\ &= |\mathcal{S}_v| \ln |\mathbf{C}_v| + |\mathcal{S}_v| \text{tr}(\mathbf{I}) \end{aligned} \quad (17)$$

where $\mathbf{I}$ is the identity matrix of the same size as $\mathbf{Z}_s$. Since $|\mathcal{S}_{vw}| = |\mathcal{S}_v| + |\mathcal{S}_w|$, all terms involving $\text{tr}(I)$ sum to zero in the final merging criterion, which becomes:

$$\begin{aligned} \partial E(v, w) = &|\mathcal{S}_{vw}| \ln |\mathbf{C}_{vw}| - |\mathcal{S}_v| \ln |\mathbf{C}_v| - \\ &|\mathcal{S}_w| \ln |\mathbf{C}_w| - \beta \sum_{s \in \partial\mathcal{S}_v \cap \partial\mathcal{S}_w} g(\nabla_s) \end{aligned} \quad (18)$$

C. Edge Strength Measure

Both the watershed transform [27] and the edge penalty function in (8) require an edge strength measure ∇_s at each site s. Two approaches for calculating the edge strength measure were considered. The first was the vector field gradient (VFG) [30] that is already used in IRGS, which works on real-valued images. VFG computes the gradient magnitude of each pixel in a real image, which can consist of one or more channels. The second approach is a polarimetric edge strength calculation that works on complex polarimetric data, e.g. [31], [32], [33].

Since the VFG calculation works only on real-valued images, preliminary tests were used to evaluate several real-valued decompositions of polarimetric data for use with VFG:

(i) The amplitude of the HH, HV and VV channels:

$$\mathbf{y}_s^{||} = \begin{bmatrix} 20 \log |S_{hh}| \\ 20 \log |S_{hv}| \\ 20 \log |S_{vv}| \end{bmatrix} \quad (19)$$

(ii) The Pauli decomposition [18]:

$$\mathbf{y}_s^{\text{Pauli}} = \begin{bmatrix} 20 \log \frac{|S_{hh} + S_{vv}|}{2} \\ 20 \log \frac{|S_{hh} - S_{vv}|}{2} \\ 20 \log (2|S_{hv}|) \end{bmatrix} \quad (20)$$

(iii) The H/α decomposition [18]:

$$\mathbf{y}_s^{\text{H}/\alpha} = \begin{bmatrix} H & \alpha \end{bmatrix}^T \quad (21)$$

where H is the entropy and α is the polarimetric scattering parameter. The H/α decomposition has previously been used for initializing unsupervised polarimetric segmentation algorithms [7].

The amplitude of the HH, HV and VV (i.e. $\mathbf{y}_s^{||}$) channels produced the best overall classification accuracy in the tests and are therefore used in the VFG computation for the results that are reported in this paper. The amplitude images have a large range of values and it was necessary to clip the values of each channel to the range of $[-40, -5]$ dB to prevent large values from dominating the range of the computed gradient. The implementation of VFG in IRGS expects data to be normalized to $[0, 255]$ and the normalization from $[-40, -5]$ dB to this range is done in floating point values to avoid quantization.

A polarimetric edge strength calculation method [31], which makes full use of the information in polarimetric data, was also evaluated, but this approach did not lead to consistent and accurate classification results. This approach computes a likelihood ratio [34], also known as the Bartlett distance [35], between pairs of pixels in different orientations as a measure of the edge strength. Parameters of the method [31] were adjusted, including the number of orientations considered, the window size for filtering and whether estimation [36] of the number of looks in each filter window is used. As none of these adjustments produced consistent results and because the VFG gradient calculated from $\mathbf{y}_s^{||}$ did generate consistent results, the VFG gradient was chosen as the edge strength measure.

D. Initialization

IRGS requires that the statistics of each class ($\mathbf{C}_i$ in (13)) be initialized before the algorithm can begin. Several approaches are possible. The $\mathbf{C}_i$ can be set to values based on a classification of a related scene and used as the initial seed values for a polarimetric K-means algorithm with the distance measure based on the polarimetric feature model [5]. Alternatively, the polarimetric matrices can be decomposed into the polarimetric H/α parameters and classified into several classes based on a pre-determined division of the H-α feature space, after which the initial $\mathbf{C}_i$ are calculated with the class labels in the H/α classification result [7]. Both of these approaches require some initial set up with *a priori* knowledge: a classification of a related scene or a pre-determined division of the H-α plane. As IRGS aims to be as automated as possible, several fully automated approaches were considered:

(i) Assign random labels to each region and compute the mean $\mathbf{C}_i$ for each class.
(ii) The initial $\mathbf{C}_i$ from approach (i) are used as the initial seed for polarimetric K-means [5] to calculate a refined set of $\mathbf{C}_i$.
(iii) Run the IRGS region-level K-means (RKM) [15] on one of:
  (a) The HH, HV and VV amplitude image from (19)
  (b) The Pauli decomposition image from (20)
  (c) The H/α parameters from (21)

  and use the obtained class labels to compute the initial $\mathbf{C}_i$.
(iv) Use the initial $\mathbf{C}_i$ from one of approaches (iii)(a) - (c) as the initial seed for polarimetric K-means [5] to find a second, refined set of initial $\mathbf{C}_i$.

Approach (iii)(a) with the amplitude of the HH, HV and VV (i.e. $\mathbf{y}_s^{||}$) channels produced the best overall results across the four image test cases described in Section IV. Thus, it is the approach chosen for finding the initial $\mathbf{C}_i$ for all results presented in this paper.

E. Spatial context parameter β choice

At the beginning of each iteration (step 3 in Fig. 1), the value of β in (8) is automatically modified to change the weighting of the spatial context model in a data driven manner, which is described in previous literature [13] [15]. Standard IRGS requires the Fisher criterion J [37, Sec. 4.10] between two classes in the intermediate classification for computing β to adapt to the class separability in the image. However, there is no Fisher criterion between classes with Wishart-distributed mean covariance matrices. Future work should investigate possible analogous measures for Wishart matrices. For the time being, β in PolarIRGS must be calculated without the Fisher criterion:

$$\beta(\tau) = c_1 \beta_0(\tau) \tag{22}$$

where τ is the iteration number to emphasize that β changes at each iteration. The value of $\beta_0(\tau)$ is calculated at each iteration to maintain the expected class boundary length at the next iteration [38] to preserve the current level of detail in the image. c_1 is a multiplier which allows the user to control the overall smoothness and level of merging of the algorithm [15]. For this paper, $c_1 = 5$ since it produced the best results. Previous experiments have found that IRGS is not particularly sensitive to c_1 [39].

F. Boundary site labeling

After the region-based label field configuration is produced, the single pixel boundary between regions remains unlabelled. Each boundary site s is labelled by choosing the label that minimizes the following energy:

$$x_s = \arg\min_{i \in \mathcal{L}} \{\ln|\mathbf{C}_i| + \mathrm{tr}(\mathbf{C}_i^{-1}\mathbf{Z}_s) + \beta \sum_{t \in \mathcal{N}_s \cap \mathcal{S}_{\text{labelled}}} (1 - \delta(i, x_t))\} \tag{23}$$

where $\mathcal{N}_s$ is the eight pixel neighbourhood of site s, $\mathcal{S}_{\text{labelled}}$ is the set of all sites that have been labelled already, and δ is the Kronecker delta function. Eq. (23) labels pixels based on their similarity to the class statistics and the labels of its neighbours and is very similar to the MLL model [26].

G. Polarimetric IRGS Algorithm

Table I lists the full PolarIRGS algorithm. The maximum number of iterations τ in Step 2 is set to 100 iterations. This has been found to be sufficient for convergence [14]. Convergence is achieved when the label field remains constant on further iterations. This is easily detected and for all tests in this paper, this occurred in fewer than 100 iterations.

IV. Data

Four-look, fully polarimetric L-band data from NASA/JPL AIRSAR of Flevoland, The Netherlands [40] is used to evaluate PolarIRGS. An red-green-blue (RGB) composite of the Pauli decomposition is shown in Fig. 2(a). PolarIRGS' unsupervised classification accuracy was evaluated by four test images shown in Fig. 2(b):

1) Mask 1: This sub-image was used by Wu et al. [10] to evaluate their Region-based WMRF technique. The ground-truth used in this paper to evaluate Mask 1 classification results is shown in Fig. 4(d) and is an approximate recreation of Wu et al.'s ground-truth as

TABLE I
ALGORITHMIC DESCRIPTION OF POLARIRGS

1. a) Compute edge strength map $\nabla = \{\nabla_s | s \in \mathcal{S}\}$ to measure edge strength at all sites using the image feature set defined in (19).
   b) Oversegment image with the watershed algorithm [27] and construct RAG with one vertex for each watershed region.
2. Let τ be the current iteration number and set $\tau = 1$. Assign a random initial label to each region and run a region-level K-means [15] on $\mathbf{y}_s^{||}$ from (19) to produce an initial unsupervised classification. From this classification, compute initial $\mathbf{C}_i$ (mean polarimetric covariance matrix) for each class.
3. a) Update β according to (22).
   b) Each vertex $v \in \mathcal{V}$ is visited once in a random order and assigned a label with Gibbs sampling [28] to minimize (7). This step moves the segmentation and classification result toward the optimal configuration. If $\tau > \tau_{max}$, go to Step 5, where τ_{max} is a user-specified maximum number of iterations.
4. a) Compute merging criterion ∂E with (18) for every pair of regions with the same label and connected by one arc in the RAG.
   b) Merge the pair with the most negative ∂E. Repeat Step 4a until all $\partial E \geq 0$.
   c) Go back to Step 3.
5. Label boundary sites using (23) to produce $\mathbf{x}$, the final label field configuration image.

the original authors could not be contacted. Evaluation of PolarIRGS on Mask 1 with a similar ground-truth as Wu et al. allows a comparison to be made between PolarIRGS and Region-based WMRF.

2) Mask 2: This sub-image is an additional test case. The ground-truth used to evaluate this sub-image is a portion of a ground-truth map (which will be referred to as GT2 in this paper) that combines ground-truth information from [41] and [35]. The portion of GT2 used for Mask 2 is shown in Fig. 5(d).
3) Mask 3: This sub-image was used to evaluate SGP by Ersahin et al. [12]. The ground-truth map used for this sub-image is also a portion of the GT2 map and is shown in Fig. 6(d). This is the same ground-truth used by Ersahin et al. for evaluating SGP. Mask 3 allows for comparison against the SGP technique.
4) Full image: The full image was evaluated by using the entire GT2 map as ground-truth. This ground-truth is shown in Fig. 7(b).

The ground-truth map used for Mask 1 and by Wu et al. [10] is a distinct version of the Flevoland ground-truth from the GT2 map (although the ground-truth maps do not contradict each other). Thus, Mask 1 is evaluated separately from the other test cases. None of the the ground-truth maps for the Flevoland data set are complete; i.e. they do not give the label for every single pixel. Therefore, accuracy statistics are computed only for pixels of known class. The legend for the ground-truth maps and classification results used in this paper is shown in Fig. 3

V. TESTING AND RESULTS

A. Evaluation Methodology

PolarIRGS was implemented in C++ as a module in the MAGIC image analysis system [42]. The algorithm was then used to segment and classify the three sub-images and the full scene shown in Fig. 2. The classification result initially does not have meaningful labels (i.e., the generic label assigned by the algorithm is not associated with the name of a ground-truth class in the legend of Fig. 3). This is due to the fact that PolarIRGS is an unsupervised segmentation and classification algorithm (see Section II-B).

To compare with published ground-truth, each generic label in the unsupervised classification result (one of $\{1, \ldots, \mathcal{C}\}$) must be associated with a ground-truth class (Stembeans, Peas, etc.). This is accomplished by finding a mapping of generic labels to ground-truth class names (i.e. label 2 maps to Stembeans, label 1 maps to Peas) that maximizes the overall accuracy, where overall accuracy is defined as the percentage of pixels with ground-truth information that are assigned to the correct ground-truth label. This mapping can be found by exhaustively trying all possible mappings of generic labels to ground-truth labels and finding the one with highest overall accuracy, although in practice this is solved by finding the mapping that maximizes the trace of the classification confusion matrix, which translates into an assignment problem [43] that can be solved by linear programming. The generic labels are assigned to ground-truth labels in this optimal fashion rather than labeling with training data so that the success of the unsupervised classification algorithm can be evaluated without introducing uncertainties due to an imperfect labeling process. As the image segments have already been given generic labels by PolarIRGS before meaningful names are assigned to each generic label, the algorithm is not using any ground-truth information to generate the classification.

The overall accuracy and the individual class accuracies (the percentage of pixels of each class correctly classified) are used as measures of the quality of a classification algorithm. The ground-truth does not provide a label for each pixel of the entire image so the accuracy calculation is limited to only those pixels where the ground-truth provides a label. Since the Gibbs sampling in Step 3 is a stochastic process [28] and because the region-level K-means initialization [15] begins with a random seed, the algorithm can produce slightly different results on each execution on the same data. Therefore, PolarIRGS was run 10 times for each sub-image and the full scene to determine the stability and consistency of PolarIRGS.

To demonstrate the benefit of including edge strength information as part of the segmentation cost function, an MLL-based version of PolarIRGS was also implemented and tested. This MLL implementation differs from PolarIRGS only in that $g(\nabla_s) = 1$ in all equations, penalizing all class boundaries equally.

B. Mask 1 Results

The mean accuracy over the 10 executions of PolarIRGS and the standard deviation of the accuracy are reported in Table II for Mask 1. MLL results are also included. The results from Wu et al.'s Region-based Wishart-MRF technique (Region WMRF) [10] are also shown in the table for comparison; these results are taken directly from [10]. The number of classes for Mask 1 was set to 8 to match the Region WMRF paper. The results in Table II show that PolarIRGS is highly successful for classifying Mask 1: the overall accuracy is 98.3%. This is higher

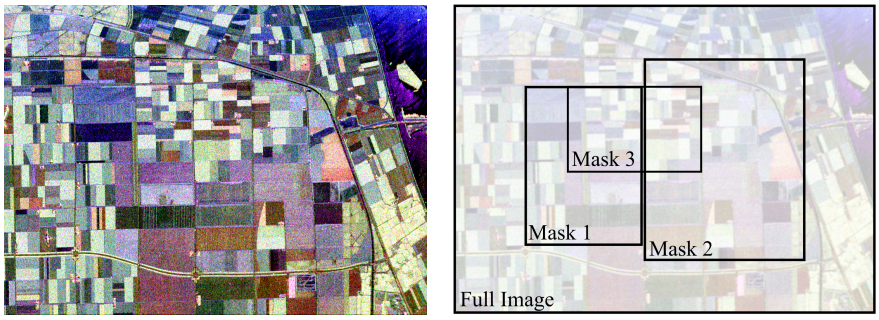

(a) Pauli RGB composite (b) Sub-images for testing

Fig. 2. The Flevoland 4-look polarimetric L-band scene. (a) The Pauli RGB composite is used to provide a partial visualization of polarimetric data. (b) The sub-images were chosen to correspond with images that were tested in previously published papers. Mask 1 was used to evaluate the Region-based WMRF segmentation technique [10] and Mask 3 was used to evaluate the spectral graph partitioning technique [12]. Mask 2 is an additional sub-image used in this paper for testing. The full image was also tested.

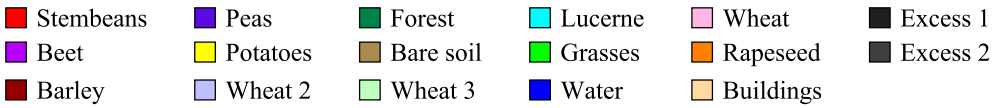

Fig. 3. Legend for ground-truth maps and classification results used in this paper. Excess classes are distinct classes in the image in regions where ground-truth information is absent.

than the MLL and Region WMRF technique, although Wu et al. [10] do not report sufficient statistics (i.e. the confusion matrix) to determine whether this improvement is statistically significant. The consistency of PolarIRGS over 10 runs of the algorithm is also excellent, with very low standard deviations across the accuracy values for all classes. In terms of individual class accuracies, PolarIRGS compares favourably with Region WMRF, improving upon Region WMRF for 4 classes, although Region WMRF outperforms PolarIRGS for the other 4 classes. However, the overall accuracy shows that PolarIRGS has an advantage.

Fig. 4 shows a classification result from one of the ten runs of the algorithm alongside the Pauli decomposition RGB and the ground-truth. Fig. 4(b) and Fig. 4(e) show the same classification result but Fig. 4(e) is masked to remove pixels where the ground-truth does not provide a label, which is how the accuracy is calculated for Table II. The classification result in Fig. 4 matches very well with the ground-truth, with most pixels being correctly classified. The figure demonstrates the effectiveness of the IRGS region-based MRF model: the segment boundaries correspond very well to the expected boundaries based on the ground-truth and each segment is contiguous and nearly noise-free. For this particular case, MLL and PolarIRGS produce results that are visually similar but PolarIRGS has higher classification accuracy.

C. Mask 2 Results

Table III reports the accuracy statistics for Mask 2 (as well as Mask 3 and the Full Image) using PolarIRGS and PolarIRGS with an MLL spatial context model. It is clear that including the edge penalty improves the accuracy compared to just using the MLL model.

Mask 2 was segmented and classified with 11 classes. Although this is larger than the number of classes in the ground-truth in the Mask 2 area, it was necessary because the ground-truth does not actually account for every single class in the scene as not all pixels are labelled; the number of true classes is higher than the number of ground-truth classes. Since PolarIRGS is an unsupervised classification algorithm, setting the number of classes equal to the number of ground-truth classes produced unreasonable results because it is not guaranteed that the classes found by the classification algorithm will correspond with the ground-truth classes. Setting a larger number of classes allows the algorithm to find the true classes in the image.

The results shown in Table III indicate that the overall accuracy for Mask 2 is lower than that of Mask 1. The high standard deviation for the accuracy of rapeseed and grasses in Mask 2 are due to a single outlier execution of PolarIRGS. The consistency and accuracy of PolarIRGS are poorer for Mask 2 than for Mask 1. The increased number of classes used for classification (from 8 to 11) makes the solution search space for the optimal configuration of labels larger, which means that the algorithm is more likely to be trapped in various local minima of (7). This results in the lower consistency (as different runs of the algorithm can be trapped in different local minima) and lower accuracy (as the local minima are not the optimal solution). However, accuracy remains at over 90% for most classes and overall.

Fig. 5 displays the classification results in the same manner as Fig. 4. Black or dark gray in the classification results indicates pixels assigned to excess classes that cannot be associated with a ground-truth class (due to setting the number of classes to 11 when there are only 8 classes in the ground-truth). These are classes found in the image but are not represented in the ground-truth labeling. The classification result shown in Fig. 5(e) compares well with the ground truth image in Fig. 5(d). Segment boundaries match accurately and the segments are contiguous and free of small segment noise. Grasses and lucerne

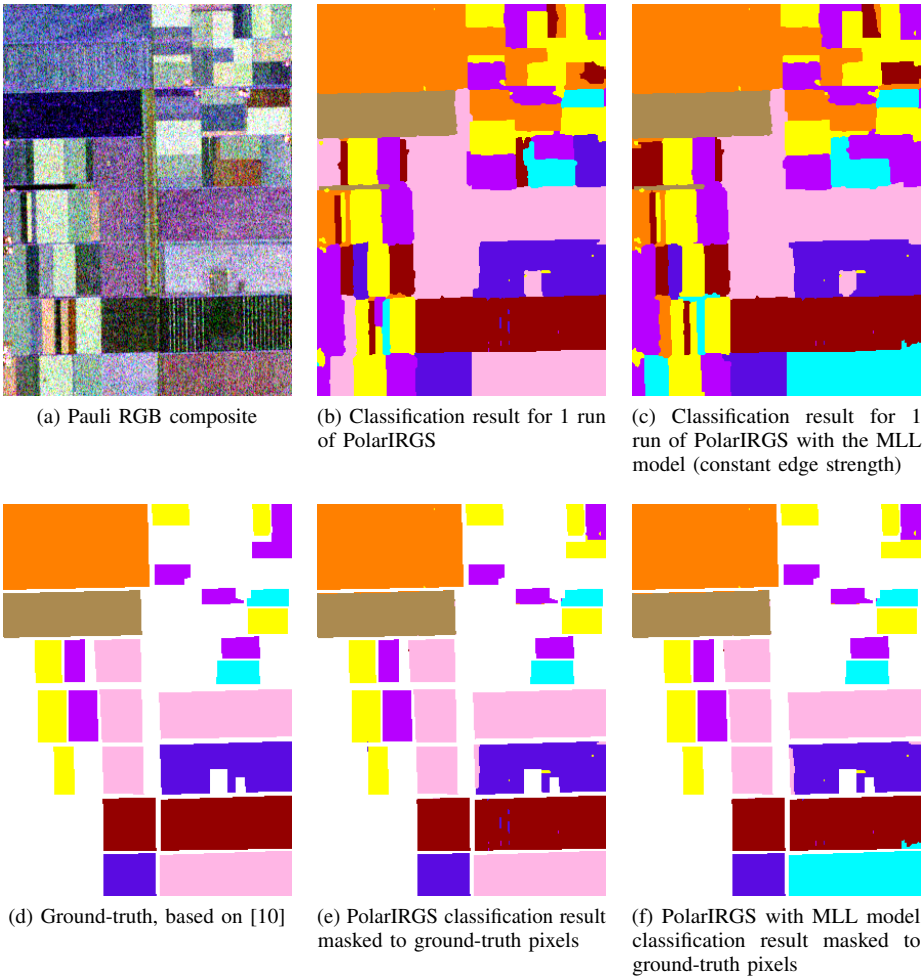

(a) Pauli RGB composite

(b) Classification result for 1 run of PolarIRGS

(c) Classification result for 1 run of PolarIRGS with the MLL model (constant edge strength)

(d) Ground-truth, based on [10]

(e) PolarIRGS classification result masked to ground-truth pixels

(f) PolarIRGS with MLL model classification result masked to ground-truth pixels

Fig. 4. Mask 1 classification results.

TABLE II

ACCURACY STATISTICS USING MASK 1 TO COMPARE POLARIRGS, POLARIRGS WITHOUT EDGE PENALTY (ONLY MLL) MODEL, AND THE REGION-BASED WISHART MRF (WMRF) SEGMENTATION TECHNIQUE [10]. POLARIRGS GENERATES THE HIGHEST OVERALL CLASSIFICATION RATE AT 98.2% WHILE THE WMRF METHOD AND THE MLL MODEL GENERATE LOWER OVERALL ACCURACIES OF 95.5% AND 91.9%.

Algorithm	PolarIRGS		PolarIRGS with MLL		Region WMRF [10]	
# of Runs	10		10		N/A	
# of Classes	8		8		8	
Class	Mean Acc.	Std. Dev.	Mean Acc.	Std. Dev.	Mean Acc.	Std. Dev.
Peas	96.7	0.1	96.3	0.75	98.4	N/A
Beet	87.6	0.2	93.6	4.3	85.3	N/A
Bare Soil	98.6	0	98.5	0.05	99.8	N/A
Rapeseed	100	0	100	0	99.2	N/A
Lucerne	99.8	~ 0	95.6	12.7	100	N/A
Wheat	100	0	77.7	15.3	90.5	N/A
Potatoes	99.9	~ 0	100	0.02	100	N/A
Barley	99.1	0.05	93.2	18.1	90.2	N/A
OVERALL	98.2	0.02	91.9	3.8	95.4	N/A

N/A = Not Applicable

TABLE III

ACCURACY STATISTICS FOR (a) POLARIRGS AND (b) POLARIRGS WITH NO EDGE PENALTY (MLL) MODEL FOR MASK 2, MASK 3 AND THE FULL IMAGE. A DASH (-) INDICATES THAT THE CLASS DOES NOT EXIST IN THE SUB-IMAGE. FOR MASK 3, POLARIRGS (84.4% OVERALL) IMPROVES OVER THE PUBLISHED SPECTRAL GRAPH PARTITIONING (SGP) SEGMENTATION [12] WHICH ACHIEVED 81.2% OVERALL ACCURACY (INDIVIDUAL CLASS ACCURACIES ARE NOT REPORTED IN [12]). THE FULL IMAGE CLASSIFICATION DOES NOT HAVE ANY KNOWN COMPARABLE PUBLISHED RESULTS FOR UNSUPERVISED CLASSIFICATION.

Sub-image	Mask 2		Mask 3		Full Image	
# of Runs	10		10		10	
# of Classes	11		9		17	
Class	Mean Acc.	Std. Dev	Mean Acc.	Std. Dev	Mean Acc.	Std. Dev
Peas	100	0	-	-	99.4	0.6
Stembeans	99.8	0.1	14.3	26.9	92	7.2
Beet	98.6	0.4	96.5	5.1	92.1	9.1
Forest	-	-	-	-	100	~ 0
Bare Soil	-	-	100	0	83.6	5.5
Rapeseed	91.4	25	0	0	33.6	7.1
Grasses	72.3	9.5	99.8	0	34.6	38.0
Lucerne	100	0	0.2	0	59.2	31.2
Wheat	89	3.9	100	0	97.6	5.2
Potatoes	99.3	~ 0	83.3	~ 0	37.7	9.6
Barley	-	-	-	-	69.2	26.0
Wheat 2	-	-	100	0	60	51.6
Wheat 3	-	-	-	-	79	23.7
Water	-	-	-	-	38.9	4.4
Buildings	-	-	-	-	93.9	1.4
Overall	91.9	0.2	84.4	0.9	69.8	4.4

(a) PolarIRGS

Sub-image	Mask 2		Mask 3		Full Image	
# of Runs	10		10		10	
# of Classes	11		9		17	
Class	Mean Acc	Std. Dev	Mean Acc	Std. Dev	Mean Acc	Std. Dev
Peas	97.7	1.8	-	-	70.2	36.8
Stembeans	92.6	0.1	11.1	27.9	71.3	16.2
Beet	91.8	6.5	81.5	16.9	65.8	15.8
Forest	-	-	-	-	99.9	0.1
Bare Soil	-	-	100	0	99.3	~ 0
Rapeseed	86.9	10.7	0	0	35.9	4.7
Grasses	85.1	26.5	99.8	0.1	38.4	28.2
Lucerne	30	48.3	0.2	0.2	66.6	23.4
Wheat	87.5	0.2	99.4	1.9	94.8	6.3
Potatoes	98.7	0.4	75.7	4	14.2	15.2
Barley	-	-	-	-	80	1.6
Wheat 2	-	-	97.4	8.2	20	42.0
Wheat 3	-	-	-	-	90	20.0
Water	-	-	-	-	43.6	6.7
Buildings	-	-	-	-	94	0.9
Overall	83.2	3.7	79.8	2.8	63.7	2.0

(b) MLL

are confused, as well as wheat and rapeseed. However, the Pauli RGB image shows that such confusion may be unavoidable: rapeseed and wheat appear similar, as do grasses and lucerne. This suggests that there may be low separability between these classes in the polarimetric data space.

Fig. 5 shows examples of the role of the edge strength model. Fig. 5(b) is the result for PolarIRGS using the edge strength model and Fig. 5(c) is the result when using PolarIRGS with the MLL model (i.e., without considering edge strength). Note the four corresponding circled regions in these two images which demonstrate how visible class boundaries are ignored by the MLL leading to erroneous region merging. (i) In the centre of the MLL image, the Excess 1 class grows across the class boundary and erroneously merges across the boundary with the adjacent Rapeseed region. (ii) In the top right, the Grasses segment is merged with Peas. (iii) At the top left corner, there are two small regions identified as Stembeans and the MLL model merges across their boundaries with Potatoes. (iv) In the bottom left, a large region of Excess 1 and a large region of Grasses are merged in the MLL case and their combined statistics relabel the class as Peas. In each of these cases, using the edge strength model preserves the class boundaries.

D. Mask 3 Results

Mask 3 was segmented and classified with 9 classes, the same as the number of classes in the ground-truth and the same number that Ersahin et al. [12] used to segment Mask 3 to evaluate their SGP technique. The overall accuracy for Mask 3

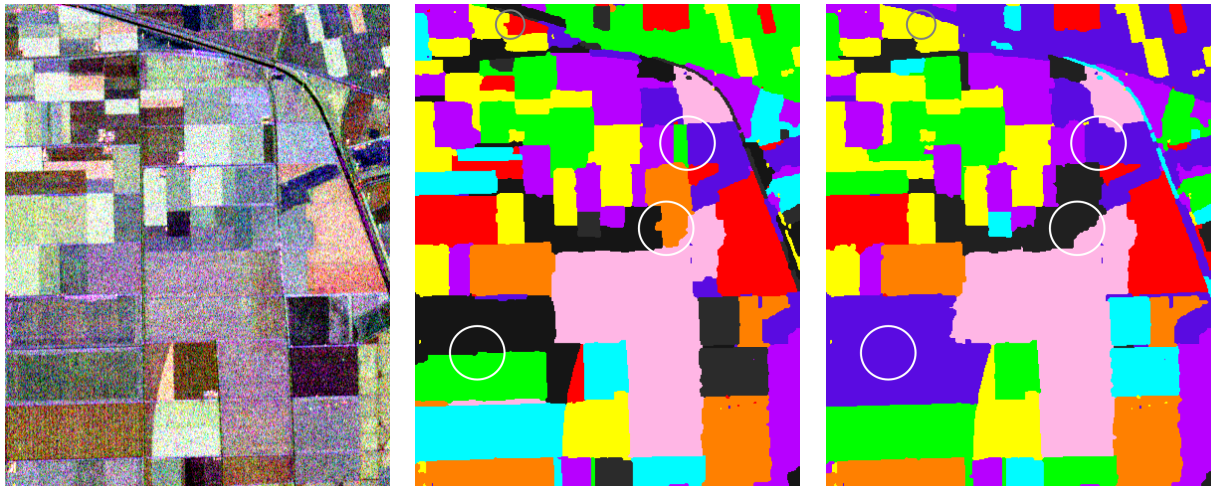

(a) Pauli RGB composite

(b) Classification result for 1 run of Polar-IRGS

(c) Classification result for 1 run of MLL

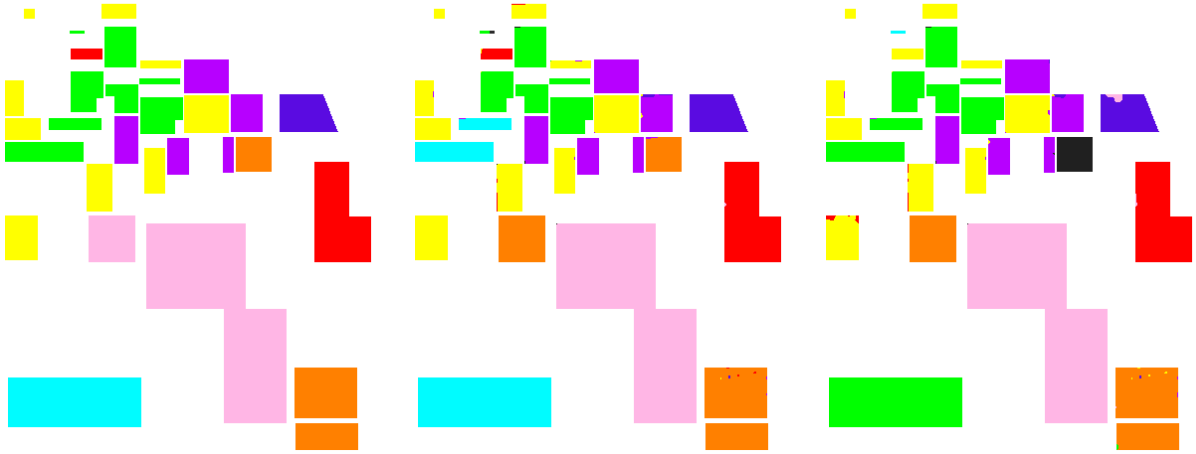

(d) Ground-truth (GT2)

(e) Classification result masked to ground-truth pixels

(f) MLL classification result masked to ground-truth pixels

Fig. 5. Mask 2 classification results with 11 classes. Black or dark gray pixels are excess classes that are not associated with any ground-truth class. Circles show locations where the MLL labeling smoothes across class boundaries while the edge strength model of PolarIRGS preserves the class boundary.

in Table III is higher for PolarIRGS as compared to MLL. The SGP technique [12] achieved an overall accuracy of 81.2%, as compared to PolarIRGS' accuracy of 84.4% for the same sub-image. Individual class accuracies were not reported for SGP. For PolarIRGS, several classes have low accuracy (Stembeans, Rapeseed and Lucerne). In Fig. 6, Rapeseed (orange in the ground-truth) was assigned the same segment as wheat (pink in the ground-truth). The lucerne (cyan) was assigned the same segment as grass, which may be unavoidable due to the very similar appearance between grass and lucerne in the Pauli RGB image (Fig. 6(a)). The lucerne that does appear in the classification result is actually an unidentified extra class that does not appear in the ground-truth. Its appearance in the Pauli RGB image is similar to potatoes but darker. The algorithm is therefore finding potatoes, dark potatoes and grass rather than potatoes, lucerne and grass. Stembeans (red in the ground-truth) in Mask 3 is grouped together with potatoes. The small patch of stembeans in the upper right of the image does not have a strong enough edge with the potato patch adjacent to it to remain separate in the IRGS model.

Although individual class accuracies are not reported in the SGP paper [12], close examination of their visual results reveal that Rapeseed and Wheat were both mislabelled as Wheat 2, which would result in near zero percent accuracy for those two classes. Lucerne is also confused with grass in the SGP paper, although some of it is classified correctly. It is expected that these classes (Rapeseed and Wheat, Lucerne and Grass) are actually quite similar in the polarimetric data space since both of these recent algorithms have trouble separating them properly.

Dramatically improving the accuracy of classifying Mask 3 is possible by using a different method of edge strength calculation and initialization. For example, when the edge strength ∇_s was calculated on the polarimetric H/α decomposition $\mathbf{y}_s^{\mathrm{H}/\alpha}$ (21) and initialization was performed using approach (ii) in Section III-D, the overall accuracy improves from 84.3% to 93.4%, stembean accuracy improves from 14.3% to 87.6%,

lucerne improves from 0.2% to 63.6% and potato accuracy improves from 83.3% to 97.7% while all other classes remain similarly accurate. The standard deviations of the accuracies are all reduced to less than 1%. These results are not emphasized to keep the edge strength calculation and initialization method consistent across tests for all three sub-images and the full-image. As mentioned in Section III-C and Section III-D, the edge strength measure and initialization method chosen for PolarIRGS are based on best overall performance across the three sub-images and the full-image. However, this test does indicate that there is potential for much better performance provided the user is willing to tune the algorithm to a specific data set.

The circled regions in Fig. 6 (Mask 3) illustrate additional cases where the edge strength model helps preserve class boundaries that are ignored by the MLL model.

E. Full Image Results

The full image segmentation and classification was performed with 17 classes as the image appeared to contain many more visually distinct classes than the previous sub-images. Table III shows that the results for the full image are worse than the previous cases, with lower accuracy and less consistency. The authors know of no other papers that reported quantitative accuracies for an *unsupervised* segmentation and classification of the *full* Flevoland scene, so it is not possible to determine the relative performance of polarimetric IRGS against other algorithms for the full image.

There are several reasons for why full image segmentation and classification produced poorer results. As explained previously, an increased number of classes leads to a larger solution space with more possibilities for the algorithm to be trapped by local minima of (7). The full image is also much larger and contains more regions to be labelled, which again increases the solution search space. The larger spatial extent of the image encompasses more classes that can be confused with each other, such as the potato and the forest class, which appear very similar in the Pauli RGB image in Fig. 7(a). This is reflected in the classification result shown in Fig. 7(d), where many of the potato pixels were grouped together into the same segment as the forest class.

Table IV shows the mean confusion matrix [44] for the full image classification across 10 runs of the PolarIRGS algorithm. This matrix was created by element-wise summing of the individual confusion matrices for each run and dividing the aggregate matrix by 10. This allows examination of which classes are frequently confused by the classification algorithm. Columns represent ground-truth classes. The numbers in each column indicate how many pixels from each ground-truth class are assigned to each of the classes in the classification result. Table IV shows that Wheat 2 and Wheat 3 are frequently confused with each other. The high standard deviation of these two classes, as seen in Table III, reflect the fact that under multiple executions of the algorithm, a pixel is assigned to one or the other class, suggesting that they are quite poorly separable. Rapeseed is often erroneously assigned to the three Wheat classes, Grasses are assigned Barley and Wheat 3, Potatoes is assigned to Forest and Water is assigned to Bare Soil and either one of the Excess classes.

Some of these segmentation and classification errors can be explained. There are several distinct signatures for Water in the scene. At the top right corner of the Pauli RGB image (Fig. 7(a)), water appears blue in the Pauli RGB composite but dark elsewhere. The bright part appears to be a wind roughening effect that causes a higher backscatter return. The confusion between Wheat 2 and Wheat 3 is due to the fact that these are actually one class (along with Wheat) that appear differently enough that they are treated as different classes by the creator of the GT2 ground-truth image. Due to their similarity, the stochastic PolarIRGS finds many different classifications that represent local minima in the solution search space. As a result, across the 10 runs of the algorithm, any given region of Wheat 2 and Wheat 3 may be assigned Wheat 2 or 3. This produces the confusion seen in the matrix. Finally, Potatoes appear very similar to Forest. Du et al. [22] grouped them together as one class since they could not be distinguished in dual-polarization data. Other authors were able to distinguish between potatoes and forest in fully polarimetric data with a *supervised* algorithm [41]. However, supervised algorithms require training data that tell the system what clusters it can expect, whereas PolarIRGS is fully unsupervised. Even with the much more challenging test case of full image segmentation and classification, the segmentation boundaries in Fig. 7(c) visually match well with the image and there is still very little noise in the segments. This indicates the strength of the region-based spatial context model inherent in IRGS.

When the classification results in the overlapping areas between Mask 1, Mask 2, Mask 3 and the full scene are compared, it can be seen that the classification results in these areas are not the same. This is because the labeling of each RAG region in a sub-image is dependent on the labeling of other regions in the sub-image due to the spatial context model. Therefore, even if two sub-images overlap, the classification result in the overlapping regions can be different due to the presence of other non-overlapping regions in the image, which affect the solution search space and the global cost function in (7). This is a fundamental property of spatial context models; the algorithm essentially considers the entire sub-image as whole when finding the classification result. This global approach helps PolarIRGS improve upon the results of other published techniques but does not guarantee that the overlapping areas will be labeled the same way in each sub-image.

However, consistency is still maintained in a number of cases. Segments classified as Beet and some segments classified as Grass are generally the same in overlapping regions in all three masks and the full image. Wheat is also consistent between the test cases if the three wheat classes are considered on class. Segments classified as potatoes are consistent between Masks 1, 2 and 3. Although the Full Mask results identify the Potato segments as Forest but as noted earlier, Potato and Forest are difficult to distinguish. In areas where the full image classification is correct, Rapeseed, Bare Soil and Peas are consistent with the Mask 1 results.

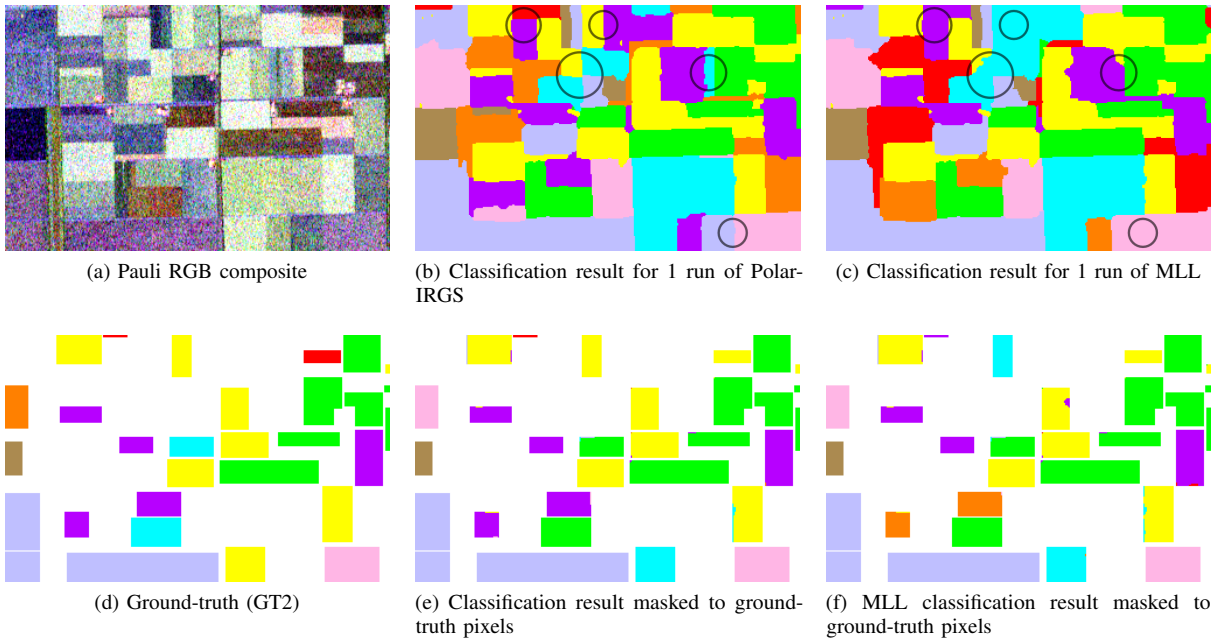

(a) Pauli RGB composite

(b) Classification result for 1 run of Polar-IRGS

(c) Classification result for 1 run of MLL

(d) Ground-truth (GT2)

(e) Classification result masked to ground-truth pixels

(f) MLL classification result masked to ground-truth pixels

Fig. 6. Classification results for Mask 3 with 9 classes. Circles show locations where the MLL labeling smoothes across class boundaries while the edge strength model of PolarIRGS preserves the class boundary.

TABLE IV

MEAN CONFUSION MATRIX [44] FOR THE FULL IMAGE SEGMENTATION ACROSS 10 RUNS OF THE POLARIRGS ALGORITHM. IT INDICATES THE GENERAL TRENDS REGARDING WHICH CLASSES ARE FREQUENTLY CONFUSED. THE COLUMNS REPRESENT GROUND-TRUTH CLASSES; THE NUMBERS IN EACH COLUMN INDICATE HOW MANY PIXELS OF THAT PARTICULAR GROUND-TRUTH CLASS WERE ASSIGNED TO EACH OF THE CLASSES IN THE SEGMENTATION RESULT.

		Ground-truth Classes														
		Peas	Stembeans	Beet	Forest	Bare Soil	Rapeseed	Grasses	Lucerne	Wheat	Potatoes	Barley	Wheat 2	Wheat 3	Water	Buildings
Segmentation Classes	Peas	10044	0	51	0	0	1	0	0	0	0	0	0	0	0	0
	Stembeans	0	6298	1	1	0	2	0	0	0	17	0	0	0	0	36
	Beet	0	6	10703	0	0	21	8	0	0	29	0	0	0	0	0
	Forest	20	320	27	18543	0	1	1	2	0	11135	0	0	0	0	0
	Bare Soil	0	0	0	0	2765	0	0	0	0	0	0	0	0	5141	0
	Rapeseed	0	0	0	0	19	4706	12	11	0	55	0	0	0	0	0
	Grasses	0	0	0	1	115	0	2585	545	0	7	1610	0	1	383	0
	Lucerne	0	0	0	0	59	0	679	6224	0	3	173	0	419	0	0
	Wheat	30	6	11	0	0	2474	1	0	17612	0	0	0	0	0	0
	Potatoes	0	27	59	0	0	0	0	2	0	6859	0	0	0	0	0
	Barley	0	0	0	1	111	0	2505	2181	0	2	5574	0	20	0	0
	Wheat 2	5	0	0	0	177	4221	11	0	442	35	518	6949	4429	0	0
	Wheat 3	2	0	0	0	0	2359	1673	1555	0	15	0	4632	18279	0	0
	Water	0	0	0	0	0	0	0	0	0	0	0	0	0	5812	0
	Buildings	6	0	2	0	0	15	0	0	0	2	4	0	0	0	572
	Excess 1	0	192	667	2	0	0	1	0	0	2	0	0	0	2196	0
	Excess 2	0	0	105	0	61	193	0	1	0	9	173	0	0	1409	0

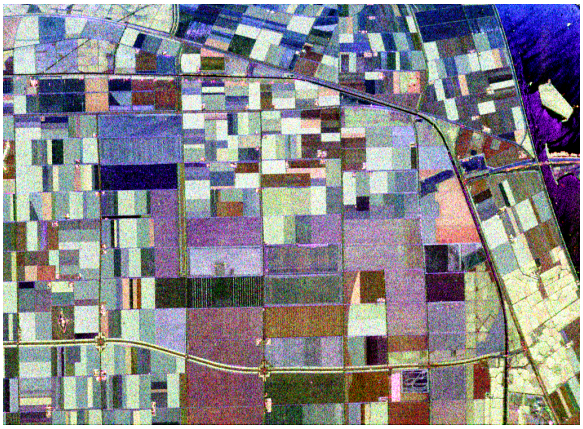

(a) Pauli RGB composite

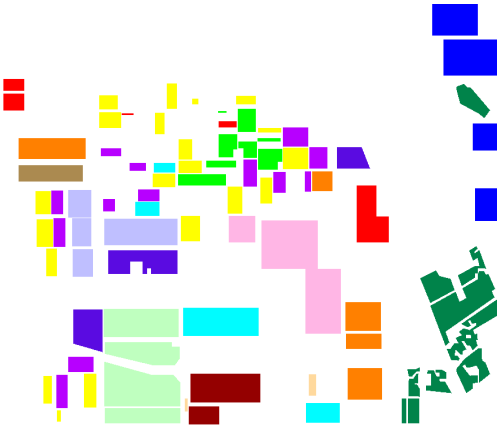

(b) Ground-truth (GT2)

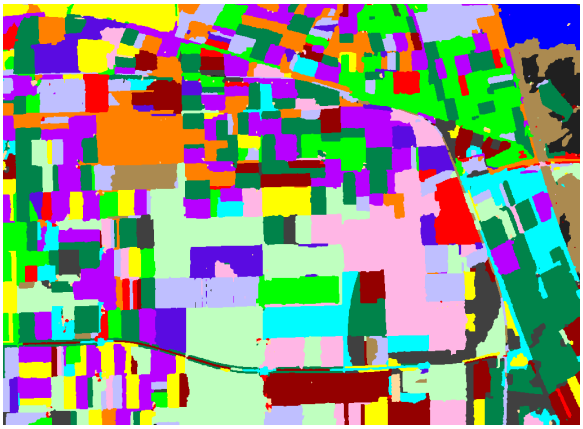

(c) Classification result for 1 run of PolarIRGS

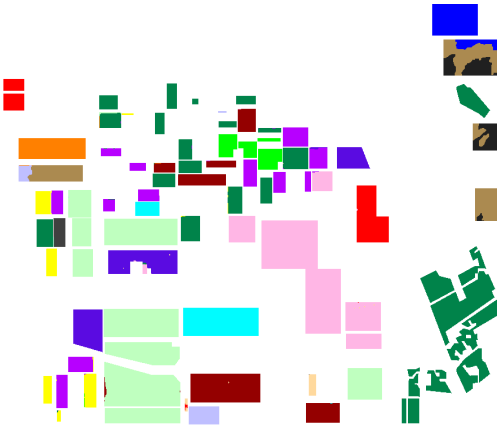

(d) Classification result masked to ground-truth pixels

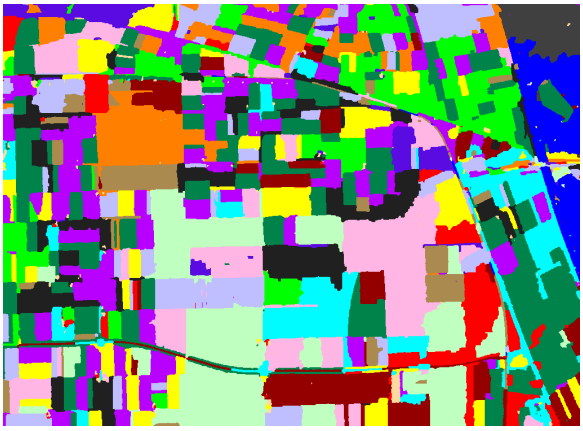

(e) Classification result for 1 run of MLL

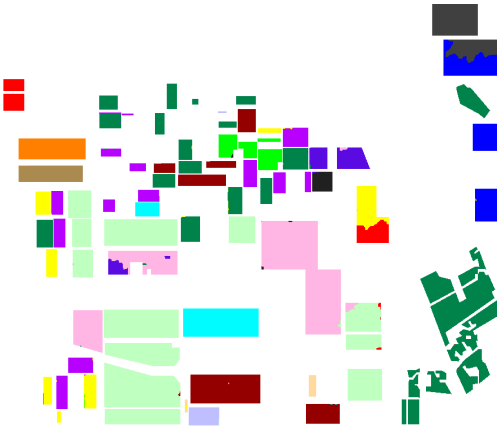

(f) MLL classification result masked to ground-truth pixels

Fig. 7. Classification results for the full image with 17 classes. Black or dark gray pixels are excess classes that are not associated with any ground-truth class.

F. Modified Full Scene Analysis

The observations made in Section V-E about the poorer accuracy of the full scene image motivate the need for a modified analysis. Poor separability and intra-class variation in polarimetric signatures make it difficult for an unsupervised algorithm like PolarIRGS to find the proper classification without *a priori* information in the form of training data that tell the algorithm what clusters it can expect. The ground-truth image and classification evaluation method was modified to account for these factors so a more reasonable evaluation of the algorithm's performance can be obtained.

The ground-truth image was modified so that only the Water in the top right corner of the image, where its signature is constant, is included in the evaluation. Wheat, Wheat 2 and Wheat 3 were grouped together as a single Wheat class. Forest and Potatoes were also merged. Fig. 8(b) shows the modified ground-truth image. The classification accuracy was evaluated on the same 17 class full image segmentation and classification

TABLE V
ACCURACY STATISTICS FOR POLARIRGS FOR THE FULL IMAGE WITH 17 CLASSES USING THE MODIFIED GROUND-TRUTH AND EVALUATION METHOD OF SECTION V-F. BY ELIMINATING CLASSIFICATION ERRORS THAT OCCUR DUE TO PROBLEMS INHERENT WITH THE DATA, A MORE REASONABLE SET OF ACCURACY STATISTICS IS OBTAINED.

Algorithm	PolarIRGS	
Sub-image	Full Image	
# of Runs	10	
# of Classes	17	
Class	Mean Acc.	Std. Dev
Peas	99.4	0.6
Stembeans	92.0	7.2
Beet	92.1	9.1
Forest / Potatoes	99.5	0.1
Bare Soil	83.6	5.5
Rapeseed	33.6	7.1
Grasses	34.6	38.0
Lucerne	59.2	31.2
Wheat (combined)	99.2	2.5
Barley	69.2	26.0
Water	99.9	0.3
Buildings	93.9	1.4
OVERALL	85.8	3.0

results that were used earlier but the three Wheat classes in the classification result were manually merged into one class. Forest / Potatoes were also merged into one combined class. This merging was done manually because there actually is more than one signature for the Wheat class and certain Potato and Forest patches are distinct. Thus, the algorithm cannot be controlled to automatically merge the classes. The classification accuracy was computed from the modified ground-truth and segmentation result.

The result of this modified analysis are shown in Table V. The accuracy has increased dramatically. Rapeseed, Grasses, Lucerne and Barley remain problematic but all other classes have high accuracies. The classification results are seen in Fig. 8(c)-(d). Accounting for the limitations inherent in the image data shows that PolarIRGS is capable of producing very reasonable classification results.

VI. CONCLUSION

This paper has presented an extension to the IRGS algorithm to use a polarimetric feature model based on the Wishart distribution. PolarIRGS is unique among polarimetric segmentation and classification techniques in that it is a region-based algorithm that incorporates edge strength between regions as part of its spatial context model and uses iterative region growing to aid in successful segmentation and classification. These properties allow it to compare favourably with and improve upon the results of other recent techniques. The region-based spatial context model is very successful at producing contiguous and noise free segments whose boundaries appear to match well with the ground-truth.

Future work should investigate improving the consistency of the algorithm between different executions for large scenes and scenes with a large number of classes. The bigger solution space associated with larger scenes and more classes appears to make it more likely for the current algorithm to be trapped in different local minima. There is potential to address this issue by investigating whether the current Gibbs sampling optimization technique could be improved or replaced with a more robust technique if one exists. Another line of future work would involve investigating measures analogous to the Fisher criterion for polarimetric data for setting the value of the spatial context weighting parameter in the PolarIRGS energy function to determine if any improvements can be made. Finally, the edge strength measure used in this paper only makes use of the amplitude information from the HH, HV and VV channels, so future work should investigate whether polarimetric edge strength measures can offer improvements once a consistent set of parameters for the polarimetric edge strength filters can be found.

ACKNOWLEDGMENT

AIRSAR imagery courtesy SIR-C CDROM (A. Freeman - NASA/JPL). The GRSS-DFC is acknowledged for providing the polarimetric image database. The authors would like to thank Prof. E. Pottier for some references and suggesting the European Space Agency's PolSARPro software, which was helpful for data conversion. The GT2 Flevoland ground-truth image was provided by Dr. S. N. Anfinsen.

REFERENCES

[1] B. Scheuchl, D. Flett, R. Caves, and I. Cumming, "Potential of RADARSAT-2 data for operational sea ice monitoring," *Canadian Journal of Remote Sensing*, vol. 30, no. 3, pp. 448 – 461, Jun. 2004.

[2] K. Nakamura, H. Wakabayashi, K. Naoki, F. Nishio, T. Moriyama, and S. Uratsuka, "Observation of sea-ice thickness in the Sea of Okhotsk by using dual-frequency and fully polarimetric airborne SAR (Pi-SAR) data," *IEEE Trans. Geosci. Remote Sens.*, vol. 43, no. 11, pp. 2460 – 2469, Nov. 2005.

[3] N. W. Park and K. H. Chi, "Integration of multitemporal/polarization C-band SAR data sets for land-cover classification," *International Journal of Remote Sensing*, vol. 29, no. 16, pp. 4667 – 4688, Jan. 2008.

[4] B. Brisco and R. J. Brown, "Agricultural applications with radar," in *Principles & Applications of Imaging Radar*, 2nd ed., ser. Manual of Remote Sensing, F. M. Henderson and A. J. Lewis, Eds. New York: John Wiley & Sons, Inc., 1998, vol. 2, ch. 7, pp. 381 – 406.

[5] J. S. Lee, M. R. Grunes, and R. Kwok, "Classification of multi-look polarimetric SAR based on complex Wishart distribution," *International Journal of Remote Sensing*, vol. 15, no. 11, pp. 2299 – 2311, Jul. 1994.

[6] B. Scheuchl, R. Caves, D. Flett, R. De Abreu, M. Arkett, and I. Cumming, "The potential of cross-polarization information for operational sea ice monitoring," in *Proc. Envisat & ERS Symposium*, Salzburg, Austria, Sep. 2004.

[7] J.-S. Lee, M. R. Grunes, T. L. Ainsworth, L.-J. Du, D. L. Schuler, and S. R. Cloude, "Unsupervised classification using polarimetric decomposition and the complex Wishart classifier," *IEEE Trans. Geosci. Remote Sens.*, vol. 37, no. 5, pp. 2249 – 2258, Sep. 1999.

[8] E. Rignot and R. Chellappa, "Segmentation of polarimetric synthetic aperture radar data," *IEEE Trans. Image Process.*, vol. 1, no. 3, pp. 281 – 300, Jul. 1992.

[9] Y. Wang, C. Han, and F. Tupin, "PolSAR data segmentation by combining tensor space cluster analysis and Markovian framework," *IEEE Geosci. Remote Sens. Lett.*, vol. 7, no. 1, pp. 210 –214, Jan. 2010.

[10] Y. Wu, K. Ji, W. Yu, and Y. Su, "Region-based classification of polarimetric SAR images using Wishart MRF," *IEEE Geosci. Remote Sens. Lett.*, vol. 5, no. 4, pp. 668 – 672, Oct. 2008.

[11] F. Cao, W. Hong, Y. Wu, and E. Pottier, "An unsupervised segmentation with an adaptive number of clusters using the SPAN/H/α/A space and the complex Wishart clustering for fully polarimetric SAR data analysis," *IEEE Trans. Geosci. Remote Sens.*, vol. 45, no. 11, pp. 3454 –3467, Nov. 2007.

[12] K. Ersahin, I. Cumming, and R. Ward, "Segmentation and classification of polarimetric SAR data using spectral graph partitioning," *IEEE Trans. Geosci. Remote Sens.*, vol. 48, no. 1, pp. 164 – 174, Jan. 2010.

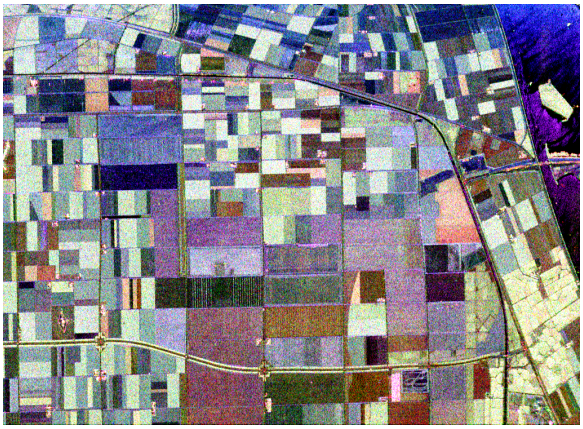

(a) Pauli RGB composite

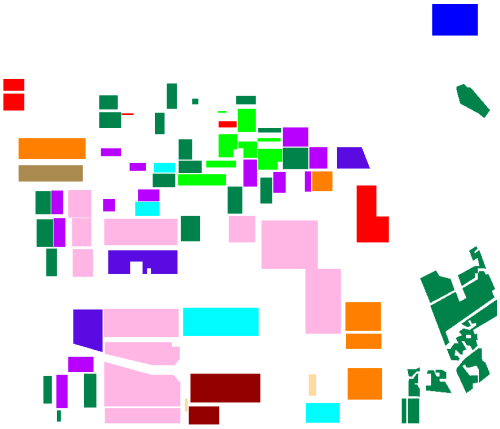

(b) Ground-truth

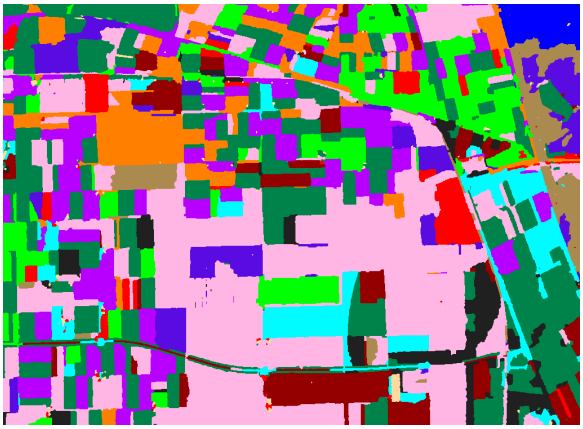

(c) Classification result for 1 run of PolarIRGS

(d) Classification result masked to ground-truth pixels

Fig. 8. Classification results for the full image with 17 classes using the modified ground-truth and evaluation method of Section V-F. Black or dark gray pixels are excess classes that are not associated with any ground-truth class.

[13] Q. Yu and D. A. Clausi, "IRGS: Image segmentation using edge penalties and region growing," *IEEE Trans. Pattern Anal. Mach. Intell.*, vol. 30, no. 12, pp. 2126 – 2139, Dec. 2008.

[14] ——, "SAR sea-ice image analysis based on iterative region growing using semantics," *IEEE Trans. Geosci. Remote Sens.*, vol. 45, no. 12, pp. 3919 – 3931, Dec. 2007.

[15] A. K. Qin and D. A. Clausi, "Multivariate image segmentation using semantic region growing with adaptive edge penalty," *IEEE Trans. Image Process.*, vol. 8, no. 19, Aug. 2010.

[16] I. S. Barbosa and P. Maillard, "Mapping a wetland complex in the Brazilian savannah using an Ikonos image: assessing the potential of a new region-based classifier," *Canadian Journal of Remote Sensing*, (submitted, Feb. 2010).

[17] Y. Boykov, V. S. Lee, H. Rusinek, and R. Bansal, "Segmentation of dynamic n-d data sets via graph cuts using markov models," in *Medical Image Computing and Computer-Assisted Intervention - MICCAI*, ser. Lecture Notes in Computer Science, W. Niessen and M. Viergever, Eds. Springer Berlin / Heidelberg, 2001, vol. 2208, pp. 1058–1066.

[18] J.-S. Lee and E. Pottier, *Polarimetric RADAR Imaging: From Basics to Applications*. Boca Raton: CRC Press, 2009.

[19] M. S. Srivastava, "On the complex Wishart distribution," *Annals of Mathematical Statistics*, vol. 36, no. 1, pp. 313 – 315, 1965.

[20] R. C. Gonzalez and R. E. Woods, *Digital Image Processing*, 3rd ed. Upper Saddle River, NJ: Prentice-Hall, 2008.

[21] S. Z. Li, *Markov Random Field Modeling in Image Analysis*, 2nd ed. Tokyo, Japan: Springer-Verlag, 2001.

[22] L. Du, M. R. Grunes, and J. S. Lee, "Unsupervised segmentation of dual-polarization SAR images based on amplitude and texture characteristics," *International Journal of Remote Sensing*, vol. 23, no. 20, pp. 4383 – 4402, Oct. 2002.

[23] M. Sonka, V. Hlavac, and R. Boyle, *Image Processing, Analysis and Machine Vision*, 3rd ed. Thompson Learning, 2008.

[24] R. Kinderman and J. L. Snell, *Markov Random Fields and Their Applications*. Providence: American Mathematical Society, 1980.

[25] Q. Yu, "Automated SAR sea ice interpretation," Ph.D. dissertation, Dept. of Systems Design Engineering, University of Waterloo, Waterloo, ON, Canada, 2006. [Online]. Available: http://www.eng.uwaterloo.ca/~dclausi/students.html

[26] H. Derin and H. Elliott, "Modeling and segmentation of noisy and textured images using Gibbs random fields," *IEEE Trans. Pattern Anal. Mach. Intell.*, vol. 9, no. 1, pp. 39 – 55, Jan. 1987.

[27] L. Vincent and P. Soille, "Watersheds in digital spaces: An efficient algorithm based on immersion simulations," *IEEE Trans. Pattern Anal. Mach. Intell.*, vol. 13, no. 6, pp. 583 – 598, Jun. 1991.

[28] S. Geman and D. Geman, "Stochastic relaxation, Gibbs distributions, and the Bayesian restoration of images," *IEEE Trans. Pattern Anal. Mach. Intell.*, vol. 6, no. 6, pp. 721 – 741, Nov. 1984.

[29] J.-S. Lee, M. R. Grunes, E. Pottier, and L. Ferro-Famil, "Unsupervised terrain classification preserving polarimetric scattering characteristics," *IEEE Trans. Geosci. Remote Sens.*, vol. 42, no. 4, pp. 722 – 731, Apr. 2004.

[30] H.-C. Lee and D. R. Cok, "Detecting boundaries in a vector field," *IEEE Trans. Signal Process.*, vol. 39, no. 5, pp. 1181 – 1194, May 1991.

[31] J. Schou, H. Skriver, A. A. Nielsen, and K. Conradsen, "CFAR edge detector for polarimetric SAR images," *IEEE Trans. Geosci. Remote Sens.*, vol. 41, no. 1, pp. 20 – 32, Jan. 2003.

[32] W. Yang, C. He, Y. Cao, H. Sun, and X. Xu, "Improved classification of SAR sea ice imagery based on segmentation," in *Proc. IGARSS*, Jul. 2006, pp. 3727 – 3730.

[33] C. J. Oliver, D. Blacknell, , and R. G. White, "Optimum edge detection in SAR," *IEE Proc. Radar, Sonar Navig.*, vol. 143, no. 1, pp. 31 – 40, Feb. 1996.

[34] K. Conradsen, A. A. Nielsen, J. Schou, and H. Skriver, "A test statistic in the complex Wishart distribution and its application to change detection

in polarimetric SAR data," *IEEE Trans. Geosci. Remote Sens.*, vol. 41, no. 1, pp. 4 – 19, Jan. 2003.

[35] S. Anfinsen, R. Jenssen, and T. Eltoft, "Spectral clustering of polarimetric SAR data with Wishart-derived distance measures," in *Proc. POLinSAR 2007*, Frascati, Italy, Jan. 2007.

[36] F.-K. Li, C. Croft, and D. N. Held, "Comparison of several techniques to obtain multiple-look SAR imagery," *IEEE Trans. Geosci. Remote Sens.*, vol. 21, no. 3, pp. 370 – 375, Jul. 1983.

[37] R. Duda, P. Hart, and D. Stork, *Pattern Classification*, 2nd ed. New York: Wiley, 2001.

[38] X. Descombes, R. D. Morris, J. Zerubia, and M. Berthod, "Estimation of Markov random field prior parameters using Markov chain Monte Carlo maximum likelihood," *IEEE Trans. Image Process.*, vol. 8, no. 7, pp. 954 – 963, Jul. 1999.

[39] P. Yu, "Segmentation of RADARSAT-2 dual-polarization sea ice imagery," Master's thesis, University of Waterloo, 2009. [Online]. Available: http://hdl.handle.net/10012/4725

[40] "IEEE GRSS Data Fusion reference database, data set GRSS_DFC_0004," 2000. [Online]. Available: http://www.dfc-grss.org/

[41] J. S. Lee, M. R. Grunes, and E. Pottier, "Quantitative comparison of classification capability: Fully polarimetric versus dual and single-polarization SAR," *IEEE Trans. Geosci. Remote Sens.*, vol. 39, no. 11, pp. 2343 – 2351, Nov. 2001.

[42] D. A. Clausi, A. Qin, M. Chowdhury, P. Yu, and P. Malliard, "MAGIC: MAp-Guided Ice Classification System," *Canadian Journal of Remote Sensing*, vol. 36, no. Suppl. 1, pp. S11 – S13, 2010.

[43] R. L. Rardin, *Optimization in Operations Research*. Upper Saddle River: Prentice Hall, 1998.

[44] J. A. Richards and X. Jia, *Remote Sensing Digital Image Analysis*, 4th ed. Berlin: Springer, 2006.